Nuclear Inst. and Methods in Physics Research, A 1049 (2023) 168036

Contents lists available at ScienceDirect

Nuclear Inst. and Methods in Physics Research, A

journal homepage: www.elsevier.com/locate/nima

Light-transport incorporated plastic scintillator response to prompt gamma-rays for use in range verification of proton therapy

A. Shahsavari, N. Ghal-Eh *, R. Izadi Najafabadi

Department of Physics, Faculty of Science, Ferdowsi University of Mashhad, P.O. Box 91775-1436, Mashhad, Iran

ARTICLE INFO

Keywords:
Proton therapy
Prompt gamma rays (PGs)
Range verification
Bragg peak
MCNPX
PTRAC
PHOTRACK

ABSTRACT

In this study, the prompt gamma-rays (PGs) produced during the interactions of proton beams of various energies have been investigated using the MCNPX2.6 Monte Carlo code. Having considered a detection setup consisting of a thick lead collimator and a commercial plastic scintillator, the event-by-event data, generated by the PTRAC card of the MCNPX code, when the scintillator is exposed to PGs have been extracted before they are used in a dedicated light transport code, PHOTRACK. The plastic scintillator response when it is moved along the phantom axis determines the flux variation of proton-induced PGs which can be further related to the longitudinal deposition energy profile of protons, *i.e.*, the Bragg curve. The present study shows that the Bragg peak location is ~3.7 cm after the PG peak for different proton energies of interest. The uncertainty in the Bragg peak location data is about 0.02 cm which can be improved by taking into account the precise electron-transport simulation details.

1. Introduction

The ionization density and energy deposition of ions in the tissue reach a maximum at the Bragg peak and then decrease very rapidly which is the basis for one of the most advanced methods of treating hypoxic and radiation-resistant tumors, called hadron- or particle-therapy [1]. The ion-induced PGs extensively leave the patient's body without considerable loss, and their emission distribution is very similar to that of the incident ions. In hadron therapy, the dose curve in the tissue is unique and well-defined which is the main reason for increasing interest in hadron therapy.

Despite the many advances that have been made in photon therapy, the almost exponential decrease in the intensity of primary photons which is connected to the nature of photon interaction with matter remains the main challenge [2]. Protons and carbon nuclei, on the other hand, deliver a large portion of their energies to the target region at the end of their paths [3]. This causes the healthy tissue around the tumor to be kept unirradiated. Moreover, the higher energy transfer of heavy charged particles than photons basically results in greater relative radiobiological effectiveness (RBE) and a very limited range in the target tissue.

Along with different methods introduced for range verification in proton therapy, such as positron emission tomography (PET) [4], PG imaging (PGI) [5], PG timing (PGT) [6], Compton camera imaging (CCI) [7] and so on, the longitudinal dose profile is achievable through the careful measurement of proton-induced PG flux, which requires a thorough knowledge of probable nuclear reactions of protons with target nuclei. In practical applications, it should be taken into account in the treatment planning for proton therapy regarding the energy transfer boundary that a 3.5% uncertainty may cause an additional margin of 0.8 cm at the depth of 20 cm [8]. The more accurately the proton range is determined, the margins considered in the proton path are reduced, and thus a lower radiation dose will reach the body.

The studies show that the hadron-induced PG emission is correlated with the dose distribution in the tissue and therefore the monitoring of these gamma-rays is known as one of the important approaches to quality assurance of proton therapy [9,10]. The radioactive nuclei are generally distributed over a relatively large volume which means that the production point of the radioactive nucleus is not the same as that of the delayed gamma-rays (*i.e.*, wash-out effect) [11]. Therefore, the consideration of the delayed decay reactions (*e.g.*, positron emission) reduces the accuracy of real-time range verification. The general consensus is that PGs along the path of protons would be a better choice. The PGs are emitted within less than 1 nanosecond and at approximately the same reaction point. The results also show that the PG fall-off curve is much closer to the actual energy deposition in the tissue than the positron-emitters ones [4]. PG emission depends on both the density and the composition of the tissue under proton-beam irradiation within the framework of proton-induced nuclear reactions, whilst the deposition energy depends mainly on the electromagnetic interactions along the proton path [12].

The focus of the present study has been on the PGs released from the target phantom, and their spectroscopy with a commercial plastic

* Corresponding author.
E-mail address: ghal-eh@um.ac.ir (N. Ghal-Eh).

https://doi.org/10.1016/j.nima.2023.168036
Received 7 November 2022; Received in revised form 23 December 2022; Accepted 11 January 2023
Available online 13 January 2023
0168-9002/

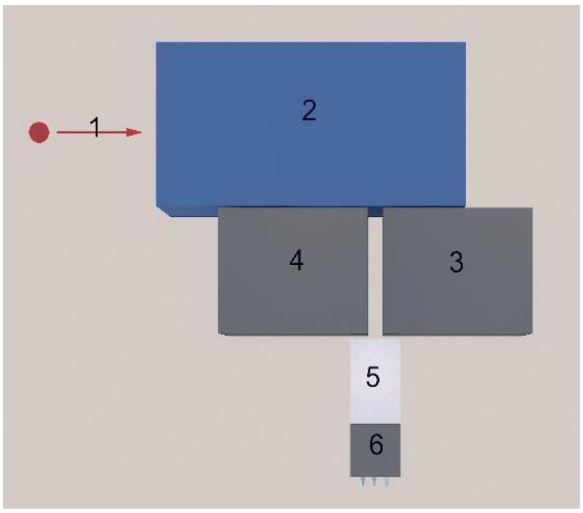

Fig. 1. The setup geometry used in the simulations. A pencil beam of protons is incident on a 15 cm × 15 cm × 30 cm rectangular water phantom and the proton-induced PGs are entered the scintillator after penetrating the narrow lead collimator: (1) Proton beam, (2) Water phantom, (3) Lead collimator (right block), (4) Lead collimator (left block), (5) Plastic scintillator, and (6) PMT.

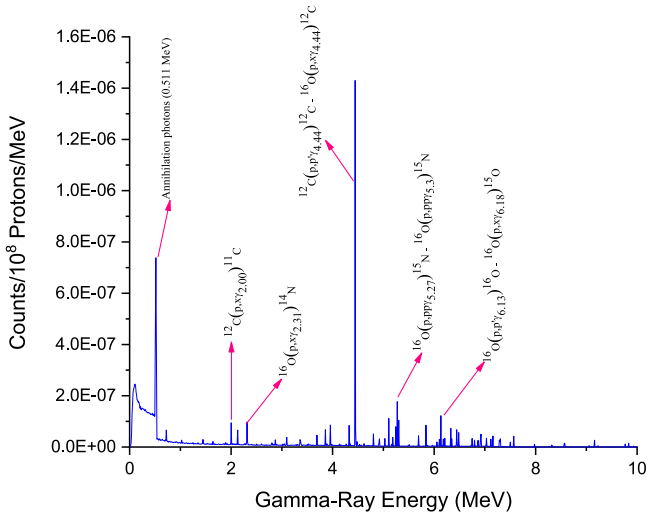

Fig. 2. The simulated energy spectrum of gamma-rays produced in the water phantom when exposed to a 150 MeV proton beam.

scintillator. The simulations have been made on the transport of PGs that can penetrate the lead collimator and reach the scintillator cell. The point-by-point deposition energy calculations (using the PTRAC card of the MCNPX code [13]), as well as the light transport modeling (with the dedicated light-transport code, PHOTRACK [14]), have been used in a post-processing program to form the scintillator response which can be a measure of the PG flux along the phantom axis. Next, the flux information is related to the proton range in the phantom and the location of the Bragg peak.

2. Materials and methods

The Bragg curve and proton range details require information about the PGs emitted from the target region following the proton interactions. The commonly used method for modeling physical phenomena is the Monte Carlo simulation. Although, there are many simulation codes such as MCNPX, FLUKA, GEANT4 and so on that are used to simulate the transport of protons inside the tissue and study secondary radiations produced in nuclear reactions [15,16], the MCNPX2.6 code was chosen due to its event-by-event output structure that could be easily coupled to PHOTRACK.

Fig. 1 represents the simplified geometry of the simulation setup where the water phantom is a 15 cm × 15 cm × 30 cm rectangular parallelepiped with the X-axis considered along the large side. The Z-axis is located in the middle of the 11.4-cm thick lead collimator where the origin of the coordinates axes coincides with the photomultiplier tube (PMT) window. Both the scintillator cell and the PMT are surrounded by a 1-mm thick aluminum layer to maximize scintillation light collection.

The major proton-induced reactions in tissue, as summarized in Table 1, are with ^{16}O and ^{12}C isotopes, both of which are also either existing or generated in the water phantom. Although there is a wide range of reaction cross-sections, only those with quite large ones are most likely to occur. Therefore, it is expected that the measured spectrum of the gamma-rays originating from a water phantom exposed to the proton beam represents several well-resolved peaks as shown in Fig. 2.

The presence of a distinct 4.44 MeV peak indicates the large cross-section of the inelastic reactions of the protons with ^{12}C nuclei (*i.e.*, $^{12}\mathrm{C}\left(p,p'\gamma_{4.44}\right)^{12}\mathrm{C}$ and $^{16}\mathrm{O}\left(p,x\gamma_{4.44}\right)^{12}\mathrm{C}$). The peak at 0.511 MeV is corresponding to the annihilation gamma-rays following the decay of positron-emitting nuclei that are also used in range-verification scenarios based on coincidence detection techniques [11]. Here, both delayed and annihilation gamma-rays have to be also carefully taken into account. The annihilation gamma-rays may have two different origins: (1) The positron annihilation events following the production of positron-emitting isotopes during the proton-induced nuclear reactions, and (2) the decay of positron-emitting isotopes following the absorption of high-energy gamma-rays. In these cases, both the positron-emitting isotopes and positrons themselves travel some distances, therefore, the proton range determination based on the detections of annihilation gamma-rays also may have some uncertainties [22]. The comparison shows that the contribution of annihilation gamma-rays is much less than those of prompt ones following the proton-induced reactions (See Fig. 3).

Table 1
PG lines and the corresponding nuclear reactions.

Target	Gamma-ray energy (MeV)	Reaction	Reference
^{12}C	2.00	$^{12}\mathrm{C}(p,x\gamma_{2.00})^{11}\mathrm{C}$	[17]
	4.44	$^{12}\mathrm{C}(p,p'\gamma_{4.44})^{12}\mathrm{C}$	[17]
^{16}O	2.31	$^{16}\mathrm{O}(p,x\gamma_{2.31})^{14}\mathrm{N}$	Foley et al. [18]
	4.44	$^{16}\mathrm{O}(p,x\gamma_{4.44})^{12}\mathrm{C}$	Foley et al. [18]
	5.27	$^{16}\mathrm{O}(p,pp\gamma_{5.27})^{15}\mathrm{N}$	Lang et al. [19]
	5.3	$^{16}\mathrm{O}(p,pp\gamma_{5.30})^{15}\mathrm{N}$	Belhout et al. [20]
	6.13	$^{16}\mathrm{O}(p,p'\gamma_{6.13})^{16}\mathrm{O}$	Foley et al. [18]
	6.18	$^{16}\mathrm{O}(p,x\gamma_{6.18})^{15}\mathrm{O}$	Narayanaswamy et al. [21]

The MCNPX simulation of the Bragg curve for the protons incident on the water phantom is carried out using two different approaches: (1) Tally F6 (or energy deposition tally) where the recorded deposition energy for the final electrons produced in the specified volumes of the water phantom perpendicular to beam axis is calculated, and (2) PTRAC card in which the event-by-event structured output is generated for further post-processing by the user.

In the MCNPX code, the so-called standard cards, such as F8 tally, provide the user with averaged or integral information, whilst the PTRAC allows the user to record all event data in an output file which will be further post-processed by the user. The interaction type, the event time and location, the energy, and the momentum vector of the particle are the main data that can be extracted from the PTRAC output. Fig. 4 shows a typical PTRAC card that may be used in the MCNPX input file, where the photon interaction data (Type=p) of 1E6 primary

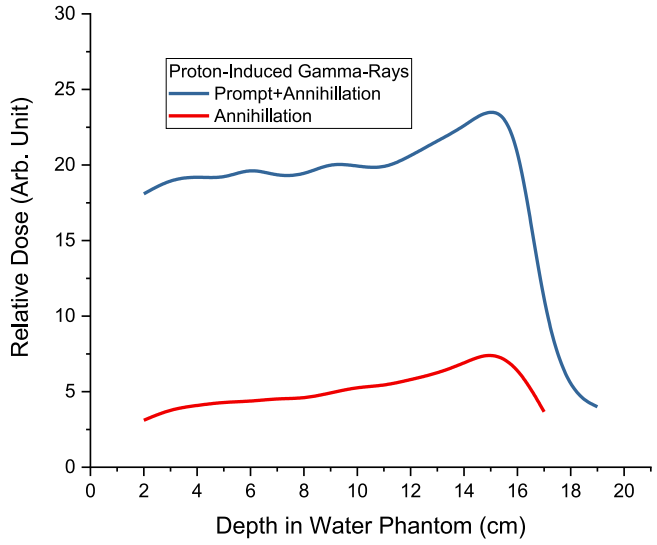

Fig. 3. The MCNPX-calculated gamma-ray intensities produced inside the water phantom along the proton beam axis for a beam of 150-MeV protons.

particles (NPS=1, 1E6) is dumped into an ASCII file. The events include collisions (col), terminations (ter), sources (src), banks (*i.e.*, secondary particle generations) (bnk), and surface crossings (sur). However, the number of events, in this case, will not exceed 1E8.

Fig. 5 shows a portion of a typical PTRAC output. Here, an event type 4000 is selected as an example, where a photon (particle ID=2) interacts with a nucleus of atomic number 53 (ZAID=Z×1000+A), and undergoes an incoherent (*i.e.*, Compton) scattering (NTYN=−1). The time and coordinates of the event, the direction of the scattered particle, and the photon energy after scattering are all recorded. Since in the present study the deposition energies of the proton-induced PGs are important to form the scintillator response, a post-processing program with the algorithm illustrated in Fig. 6 has been developed to receive the PTRAC output file and track all relevant events to filter the desired ones before the deposition energies and their corresponding locations are determined.

As can be seen in the flowchart of Fig. 6, the PTRAC output file is read by the post-processing program before all events data are sorted out to specify the deposition energy and coordinates of each gamma-ray event in the scintillation detector. Then, the Monte Carlo code, PHOTRACK, simulates the transport of the scintillation lights, originating from each energy-deposition point until they either reach the PMT or are lost due to the scintillator bulk absorption or escape. Moreover, the wavelength dependencies of the optical parameters have been carefully considered throughout the light transport simulations. The major wavelength-dependent optical parameters are (1) Scintillation light emission curve, (2) Paint reflectivity, (3) Refractive index, (4) Light attenuation coefficient, and (5) Quantum efficiency.

To verify the post-processing program, the simulation is performed with an NE102 scintillator exposed to a photon beam of 4.44 MeV energy. Fig. 7 illustrates the deposition energy spectrum of the scintillator using two different approaches (*i.e.*, F8 tally and post-processed PTRAC data), which exhibits a very good agreement. Fig. 7 confirms that the post-processing program has taken into account all necessary deposition-energy events. It should be noted that 1 MeVee or 1 MeV electron equivalent is the energy of a charged particle that produces equal scintillation light that 1 MeV electron does.

The detection setup with the geometry shown in Fig. 8 is used for the simulation study where the gamma-rays emitting along the direction perpendicular to the proton beam are detected by the plastic scintillator. It should be noted that a very small number of gamma-rays may reach the scintillation detector which results in a relatively large uncertainty. To resolve this problem, different variance-reduction techniques have been implemented in the MCNPX simulations. Using the DXT card, a small sphere with a certain radius is defined around the region of interest where more incident gamma-rays are favorable. This will force the desired gamma-rays to enter that detector and consequently improve the counting statistics. The weight-window card has been also used to manage the so-called particle weights within different regions of the measurement setup which again eventually results in more photons in the detector region. However, in both approaches mentioned above, there is a chance for errors in the simulations to occur because the particle transport has been changed to increase statistics.

It is also worth noting that using the so-called advanced surface source method in MCNPX, where the problem is divided into two separate phases (*i.e.*, phase 1: from proton source to gamma-ray production, and phase 2: from gamma-ray production to the detection), is not applicable in this case. Because this method works only for spherical geometries, whilst the phantom, which is a volumetric source of gamma-rays, is rectangular in the present study. The straightforward way to increase the number of gamma-rays reaching the detector and reduce the counting error is to use an extremely large number of histories which itself needs a very long computer run. For example, the number of 1.5E9 histories has been recorded with an Intel Core i9-7900 CPU @ 3.30 GHz, 32 GB RAM desktop computer in 350 h.

To investigate the PGs produced inside the phantom along the path of the proton beam, one has to move the collimator, each time, near the water phantom and along the path parallel to the beam to simulate the corresponding detector response. The MCNPX code has been run for 35 different points along the phantom axis, each for 3E9 primaries (*i.e.*, protons). For the sake of simplicity, both the proton source and water phantom have been moved backward instead of moving the collimator and detector set in the forward direction. This also facilitates the post-processing of the PTRAC output file because in all simulations in the present study it is assumed that the origin of cartesian coordinates is fixed and located at the scintillator-PMT boundary.

The simulations confirm that the majority of the gamma-rays incident on the detector are those produced as a result of proton reactions with the nuclei in the water phantom. However, other radiations may enter the detector (*e.g.*, neutrons from proton-induced reactions) which are very few, but they must be prevented from entering the detector as much as possible (*e.g.*, by using a thin layer of neutron-absorbing material).

3. Results and discussion

The deposition energy spectra calculated with two different approaches are shown in Fig. 9 when the NE102 scintillator is exposed to the gamma-rays produced in the water phantom of Fig. 8 as it is irradiated with a beam of 150 MeV protons. The agreement between the two spectra shown in Fig. 9 confirms the capability of the post-processing program to precisely take into account the deposition energy data.

```
PTRAC    nps=1,1E6 TYPE=p  file=asc  write=all  event=col,ter,src,bnk,sur
         CELL=1 max=1E8
```

Fig. 4. A typical PTRAC card used in the input file of the MCNPX code.

History No Event Type Cell Number
1406 1000 1
Event Type Source Type Particle Type
3000 1 40 2 0 0
X Y Z U V W Energy Weight Time
0.00000E+00 0.00000E+00 0.60000E+01 -0.88432E-01 -0.29607E-02 -0.99608E+00 0.10000E+01 0.10000E+01 0.00000E+00
4000 2 11.2 174 1 1 0
-0.44390E+00 -0.14862E-01 0.10000E+01 -0.88432E-01 -0.29607E-02 -0.99608E+00 0.10000E+01 0.10000E+01 0.16744E-01
3000 2 53000 -1 1 1 1
-0.48268E+00 -0.16160E-01 0.56326E+00 0.82874E+00 0.32176E+00 -0.45789E+00 0.45256E+00 0.10000E+01 0.18206E-01
3000 3 11.3 62 2 0 1
0.53678E+00 0.37964E+00 0.00000E+00 0.82874E+00 0.32176E+00 -0.45789E+00 0.45256E+00 0.10000E+01 0.22310E-01
5000 4 99 1 3 0 1
0.83497E+01 0.34130E+01 -0.43167E+01 0.82874E+00 0.32176E+00 -0.45789E+00 0.45256E+00 0.10000E+01 0.53756E-01
9000 4 1 1 3 0 1
0.83497E+01 0.34130E+01 -0.43167E+01 0.82874E+00 0.32176E+00 -0.45789E+00 0.45256E+00 0.10000E+01 0.53756E-01

Fig. 5. A portion of a typical PTRAC output. The letters are added to the file for better clarification.

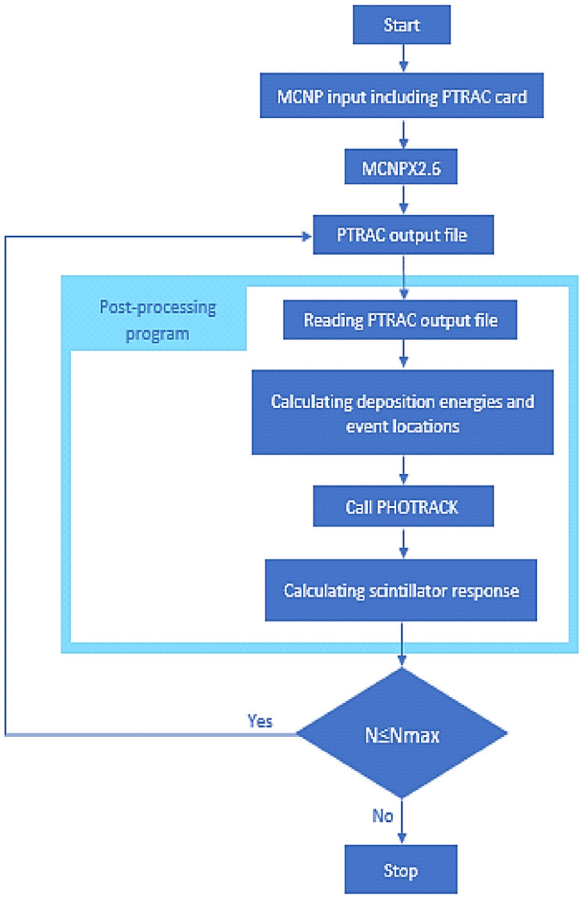

Fig. 6. Flowchart of a post-processing program for modeling the plastic scintillator response when exposed to the proton-induced PGs.

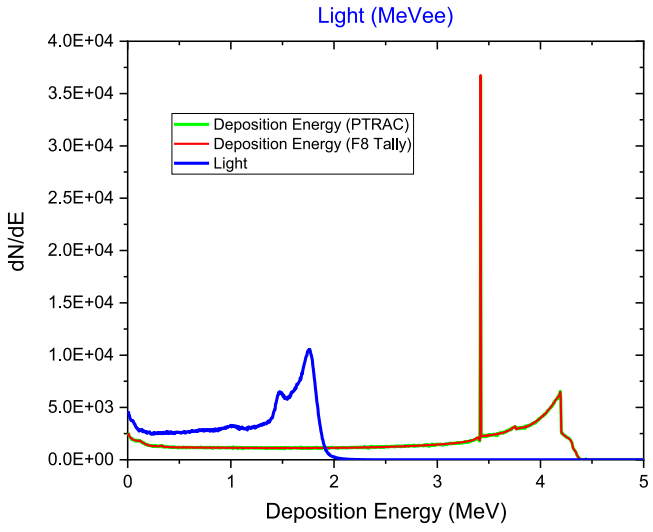

Fig. 7. The deposition energy spectrum of an NE102 scintillator (5 cm × 5 cm × 8 cm) when exposed to a 4.44 MeV photon beam using two different calculation approaches. The light spectrum calculated with MCNPX-PHOTRACK code was also illustrated for comparison.

Having performed the so-called volume flux (*i.e.*, Tally F4) calculations, the proton flux along the axis of the rectangular water phantom is obtained (See Fig. 10). As can be seen in Fig. 10, the calculated volume flux is slowly-varying before the Bragg peak region. A slight decrease in the volume flux of proton-induced PGs may be attributed either to the escape or the absorption events along the proton path. However, a sharp decrease in the proton flux is seen after the Bragg peak location. Fig. 10 also confirms that the photon flux increases with increasing beam penetration depth in the water phantom and reaches a maximum in the region just before the Bragg peak. The reason for this photon flux behavior is connected to the increase in the number of interactions as protons penetrate more in the phantom and fall off at the end of the

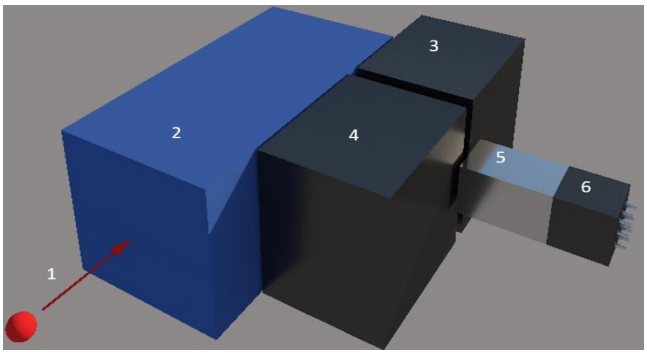

Fig. 8. The detection setup used for the simulation study which includes: (1) Proton beam, (2) Water phantom, (3) Lead collimator (right block), (4) Lead collimator (left block), (5) Plastic scintillator (NE102), and (6) PMT.

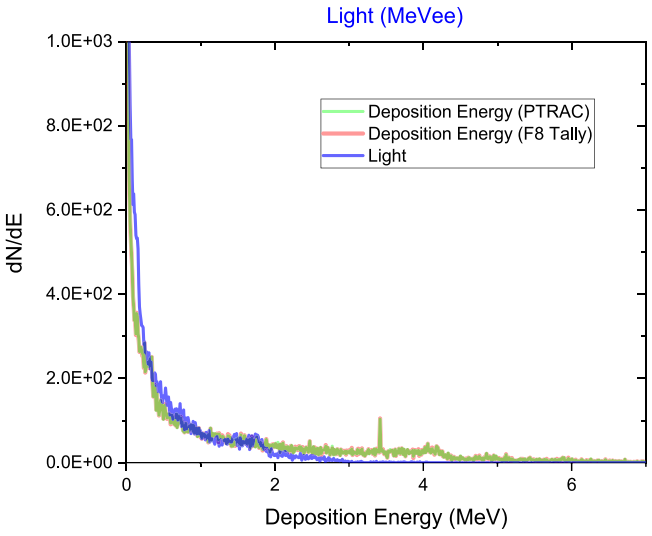

Fig. 9. Deposition energy spectra calculated for an NE102 scintillator (5 cm × 5 cm × 8 cm) exposed to the PGs produced inside a water phantom for an incident 150-MeV proton beam, using two different approaches (*i.e.*, F8 tally and PTRAC card analysis). The light spectrum, calculated with the MCNPX-PHOTRACK code, was added for comparison.

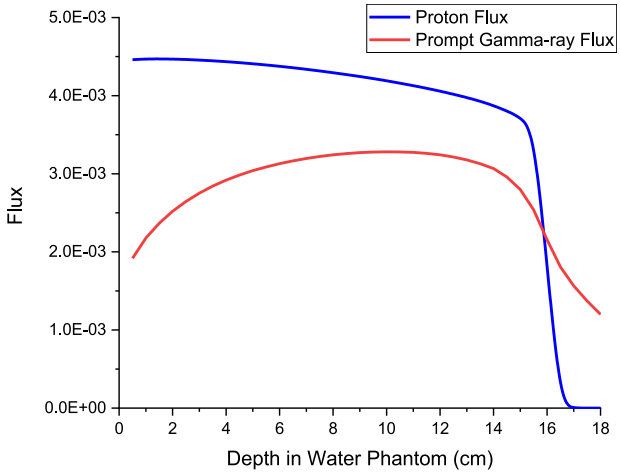

Fig. 10. Longitudinal profiles of proton and gamma-ray fluxes in a water phantom when it is exposed to a 150 MeV proton beam.

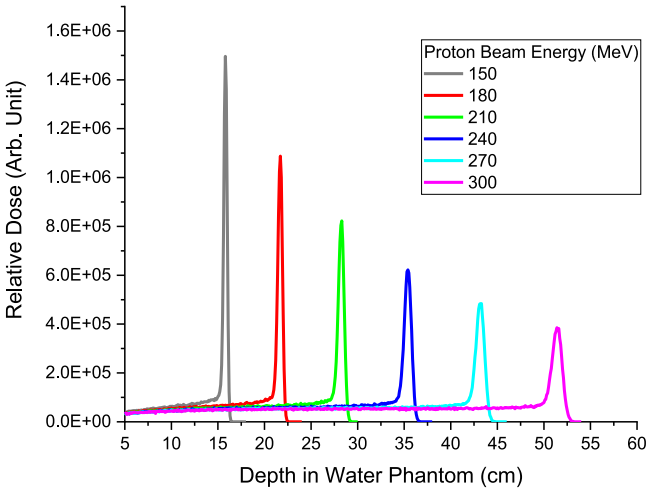

Fig. 11. The Bragg curves calculated for the proton beams of different energies when they are incident on a rectangular water phantom.

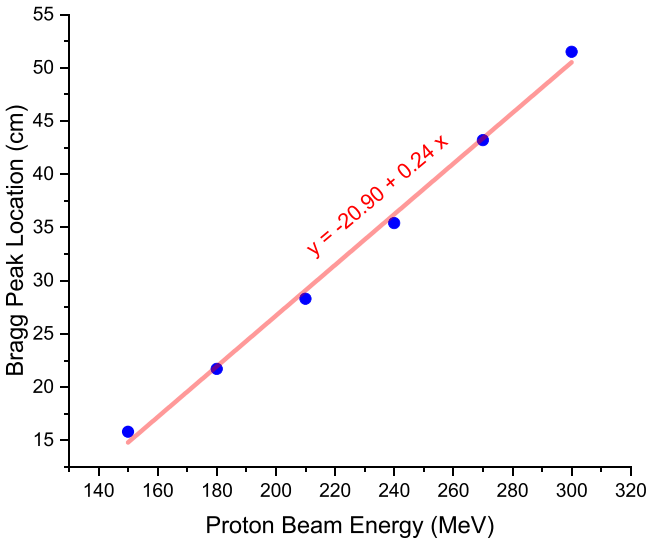

Fig. 12. Variation of the Bragg peak location as a function of proton beam energy and the corresponding linear fit.

paths. To investigate this relationship, the water phantom is exposed to the proton beams of different energies and the corresponding Bragg curves are shown in Fig. 11.

The MCNPX simulation study shows that the penetration depth or the Bragg peak location almost linearly increases with proton energy as seen in Fig. 12.

Next, the Bragg peak broadening at different energies has been investigated. The results confirm that by increasing the proton beam energy, both the penetration depth and the width of the Bragg peak are increased (see Fig. 11). As expected, the beam divergence increases with increasing penetration depths (see Fig. 13). As seen in Fig. 14, the full-widths at half maxima (FWHM) are plotted against the proton beam energy with an almost linear behavior.

The angular distribution of the produced gamma-rays outgoing the water phantom is important when analyzing the proton range in the water phantom. Three different regions of the water phantom have been considered for this simulation study: (1) Front surface (*i.e.*, entrance region), (2) Before the Bragg peak location (*i.e.*, plateau region), and (3) Bragg peak location. To this purpose, the geometry of Fig. 15 (*i.e.*, a rectangular water phantom) has been considered for the MCNPX simulations.

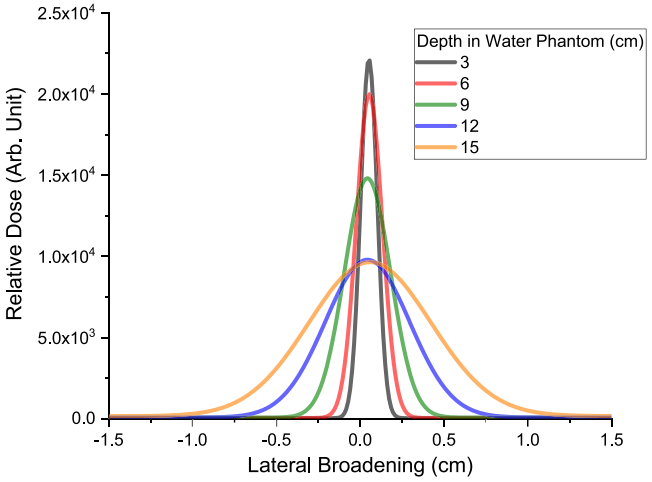

Fig. 13. The divergence of a 150 MeV proton beam at different depths of the water phantom.

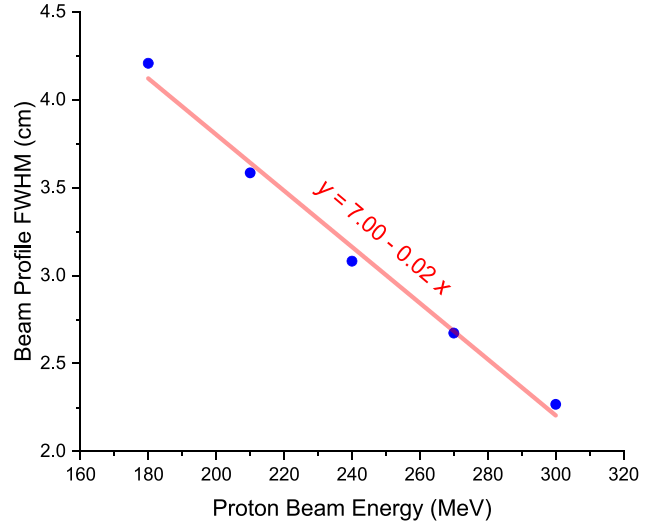

Fig. 14. Variation of beam profile broadening (*i.e.*, FWHM) at the depth of 12 cm in the water phantom versus proton beam energy.

The gamma-ray flux emerging from each slice has been calculated and then plotted in Fig. 16. As shown in Fig. 16, the proton-induced PGs leaving the phantom surface are symmetrically emitted with respect to the direction perpendicular to the incident proton beam. The simulations also confirm that the mean proton energy decreases very rapidly inside the water phantom as shown in Fig. 17.

Having successfully incorporated the light transport simulation into the PTRAC output for generating the plastic scintillator response, it has been decided to model the main geometry of the problem, where the incident radiations are the proton-induced gamma-rays. Fig. 18 represents both the deposition energy and light spectra simulated for the plastic scintillator exposed to the proton-induced gamma-rays emerging from the water phantom. As expected, adding the light transport feature to the simulation has shifted the whole spectrum to lower amplitudes and also broadened the peaks.

Furthermore, to evaluate the contribution of the photons originating from the interactions that occur inside the collimator, which are mainly generated through proton- or neutron-induced reactions, the importance card of the MCNPX code has been set to zero for the whole collimator cell. As can be seen in Fig. 19 the comparison confirms that the contribution of the gamma-rays coming from the collimator is not negligible and must be taken into account in the proton range verification studies.

As mentioned earlier, the motivation of the present study is to determine the Bragg peak location in terms of the plastic scintillator response to proton-induced PGs when located at different positions along the water phantom axis. This requires an appropriate mathematical model to be implemented as discussed in the following. Fig. 20 shows the areas under the plastic scintillator responses when exposed to PGs at different locations along the phantom axis. The question is whether or not the number of gamma-rays detected by the scintillator reaches its maximum when the collimator is exactly located at the Bragg peak position.

As suggested by Janssen et al. [12], the penetration depth is defined as the location where the Bragg curve reaches 90% of its maximum (R90). They also show that R90 is located at the average distance taken on the minimum and maximum values of the number of PGs registered by the detector. The simulation data of the present study, when the light transport is not included (*i.e.*, when the deposition energy spectrum is taken as equivalent to the detector response), show that the difference between the penetration depth (R90) and the results of the PG data is about 0.02 cm, which is a good agreement.

The simulation data for a tissue phantom exposed to a 150 MeV pencil proton beam are shown in Fig. 21 and the corresponding results are summarized in Table 2. In Fig. 22, the area under the PG spectrum recorded by the plastic scintillator (PG) is compared with the percent depth dose (PDD) for the same penetration depth. An appropriate mathematical model in the form of a sigmoid function has been used for non-linear curve-fitting on the PG data. Next, the maximum and minimum of the curve are simply calculated.

According to Table 2, the Bragg curve reaches 90% of its maximum at the depth of 18.08 cm which is considered the penetration depth of the beam according to the definition mentioned above, whilst the

Table 2
Range estimation for a beam of 150 MeV protons incident on a tissue phantom, based on the deposition energy data.

PG	Max	Min	Average	R (cm)
	1.14E−6	1.69E−7	6.54E−7	18.1
PDD	Max	R90	–	R (cm)
	1.21E−6	1.09E−6	–	18.08

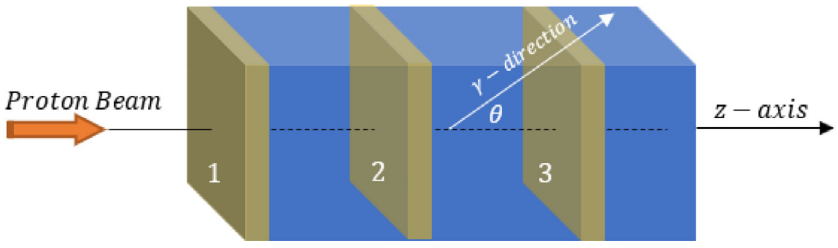

Fig. 15. The geometry of the water phantom: (1) Entrance region, (2) Plateau region, and (3) Bragg peak region. The angle θ gives the exiting gamma-ray direction with respect to the beamline (*i.e.*, z-axis).

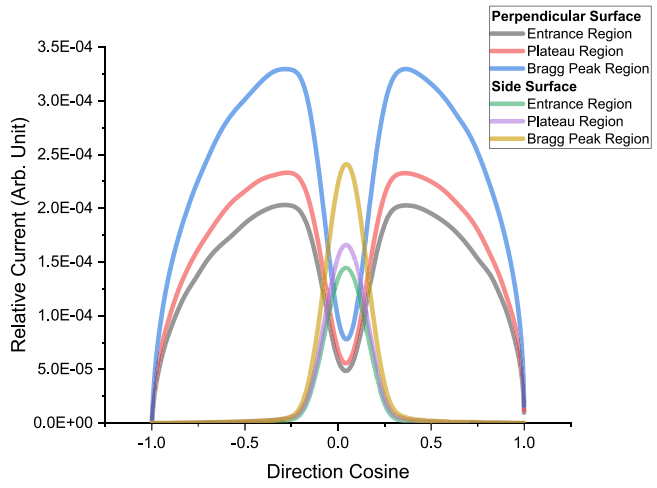

Fig. 16. Angular distribution of PGs produced following the interactions of a 150 MeV proton beam in the water phantom. The zero angle is set in the vertical direction.

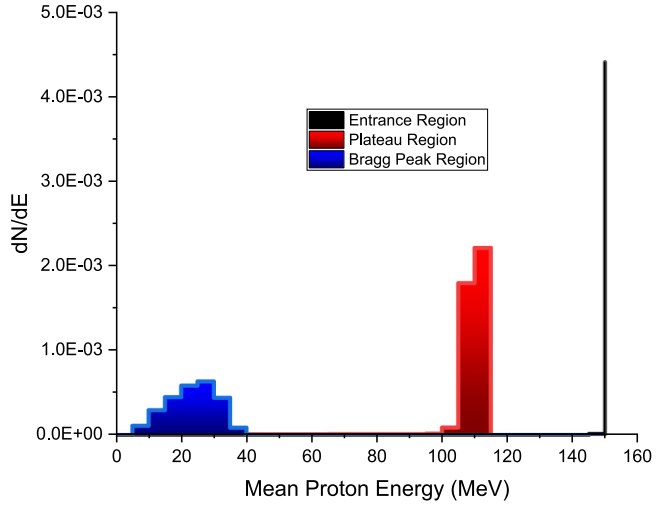

Fig. 17. Mean proton energy at different regions of the water phantom irradiated with a 150 MeV proton beam.

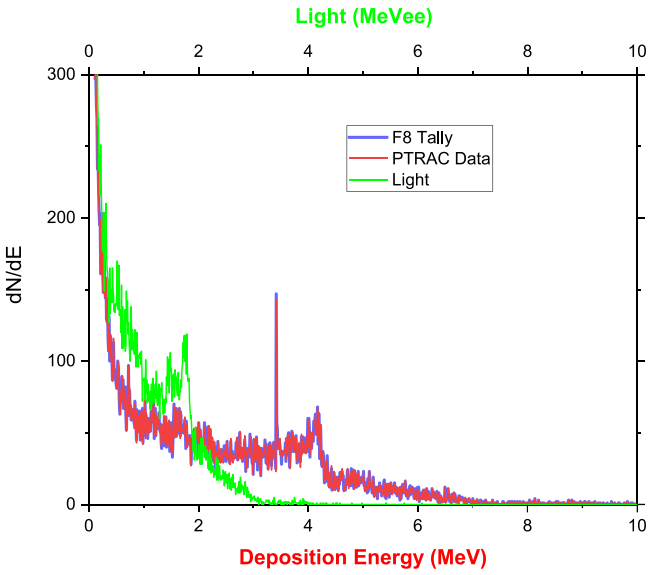

Fig. 18. The response of 5 cm × 5 cm × 8 cm rectangular plastic scintillator to PGs generated by a beam of 150-MeV protons: Deposition energy spectra (calculated with F8 tally and PTRAC data) versus light spectrum (simulated with MCNPX-PHOTRACK code).

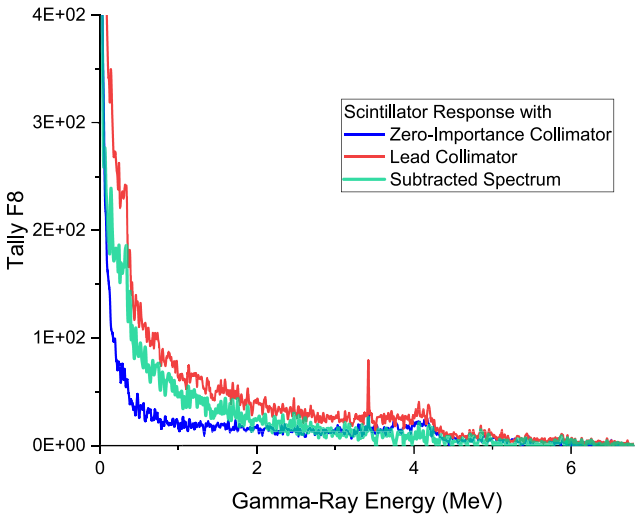

Fig. 19. The contribution of the PGs produced inside the lead collimator in the 5 cm × 5 cm × 8 cm rectangular plastic scintillator response when the water phantom is irradiated by a 150-MeV proton beam is shown as the subtracted spectrum.

average taken on the maximum and minimum of PGs data gives the depth of 18.1 cm, which represents a very good agreement.

Having added the light transport to the Monte Carlo simulations, the new set of PG data corresponding to more realistic plastic scintillator responses are shown in Fig. 22. As already expected, the maximum PG data occurs in some depths before the Bragg peak.

4. Conclusions

The present work aims to determine the location of the maximum energy deposition made by therapeutic proton beams of different energies inside water or soft tissue phantoms using Monte Carlo simulations. The underlying proton interactions with target nuclei are the key information necessary for the above simulation work. The results confirm that the proton beam diverges (Fig. 13) and the beam energy decreases (with the behavior shown in Fig. 17) as it penetrates the phantom material. Moreover, the energies of the most proton-induced PGs are less than 2 MeV (Fig. 9), which means that the detection system should have appropriate detection efficiency in this energy range.

Fig. 10 shows that the proton flux exhibits a slight decrease before the Bragg peak region, which means that a small fraction of the proton flux undergoes deflection or absorption in most of the proton track. However, an abrupt flux decrease is observed when the proton energy is sufficiently small. This means that the majority of the beam energy is carried to the track end. The produced PGs, on the other hand, reach the maximum just before the Bragg peak, as seen in Fig. 22.

Among all the possible interactions along the proton track as well as the secondary interactions that may generate different particles, the analyses prove that the events with the highest interaction cross-sections dominate and can be used for the practice of proton range verifications. The detections of the proton-induced gamma-rays that originate from the phantom are the most appropriate tool for monitoring the penetration of the proton beam inside the material because the emission time-scale of these gamma-rays is on the order of nanoseconds or less, during which the motion of the excited nuclei can be ignored.

Positrons are produced in the water phantom during the decay of positron-emitting nuclei generated by the proton interactions with

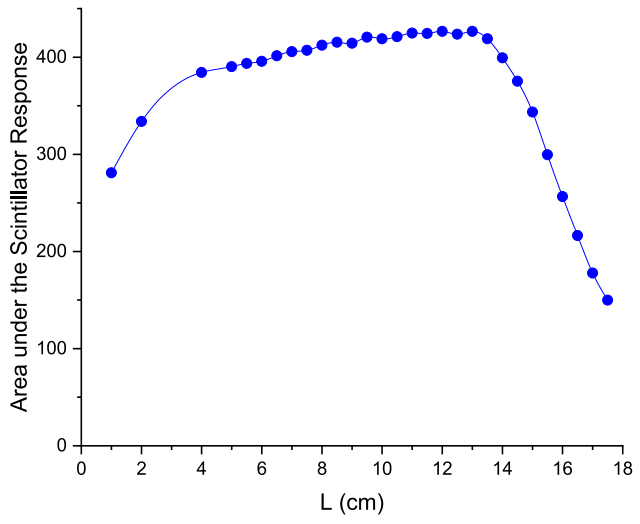

Fig. 20. The area under the scintillator response to PGs induced by 150-MeV protons in a water phantom. The data points are corresponding to different distances of the scintillator from the front surface of the water phantom (L) as shown in Fig. 2.

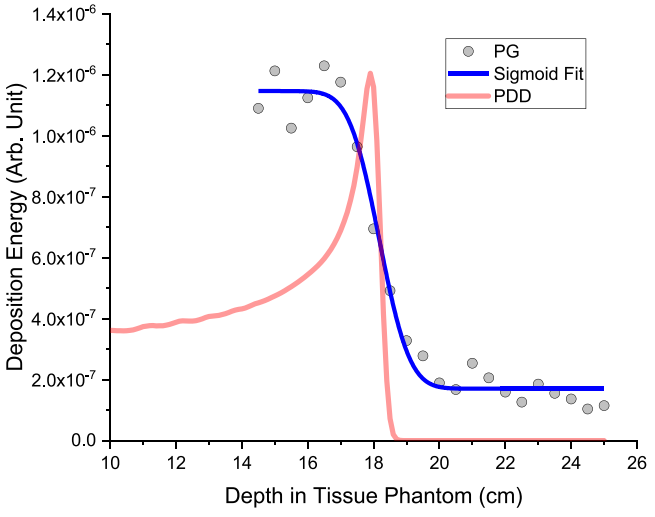

Fig. 21. A comparison of the longitudinal profile of proton-induced PGs (PG), percent depth dose (PDD), and a fit to PG data points, when a tissue phantom is exposed to a 150 MeV proton beam.

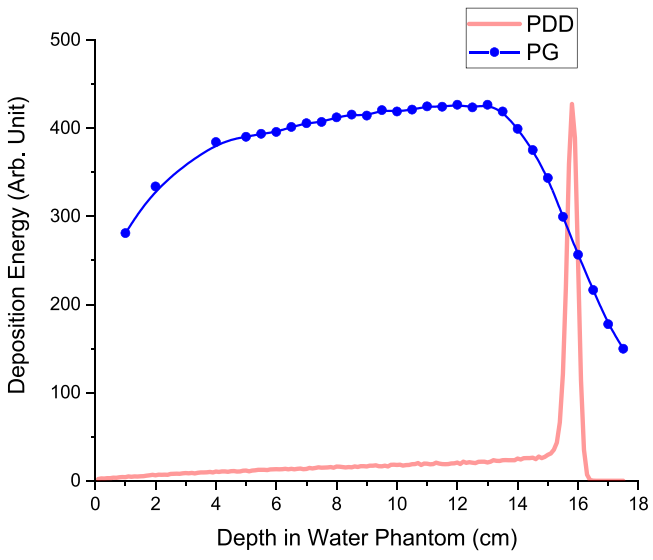

Fig. 22. Variation of the areas under the plastic scintillator responses to the proton-induced PGs (PG) compared with the Bragg curve (PDD), when a 150 MeV proton beam is incident on the water phantom.

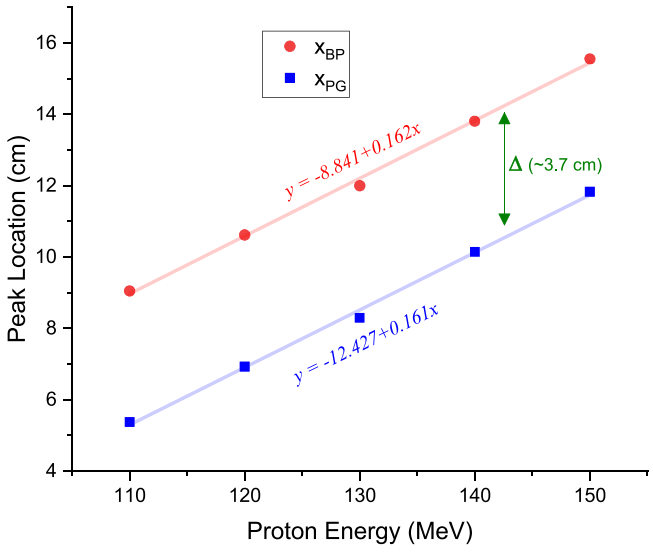

Fig. 23. Distance between Bragg peak and the location of the maximum PG for different proton energies, and the corresponding linear fits.

target nuclei as well as those in the pair-production events initiated by higher-energy PGs. The detection of 0.511 MeV gamma-rays following the positron annihilation in the medium is also considered an important proton range verification method. However, due to the considerable motions of positron-emitting nuclei before undergoing annihilations (known as wash-out), the information obtained from this method seems to be less accurate than the one based on PGs for Bragg peak determination. Moreover, the number of produced 0.511 MeV gamma-rays is much fewer than the prompt ones (See Fig. 3), which results in poor counting statistics in both measurements and simulations.

The comparison among various methods confirms that the PG flux is the most suitable measure for use in proton range verifications. However, the secondary charged particles and neutrons produced as a result of proton interactions in the water phantom and also the gamma-rays produced in both the lead collimator and detection system may cause complexities in the problem that should be carefully taken into account. For example, Fig. 19 shows that the contribution of the gamma-rays produced in the lead collimator in the plastic scintillator response is not negligible. Therefore, the scenarios for suppressing all secondary radiations except proton-induced PGs are necessary to be implemented.

It is anticipated that the longitudinal profile of the detected PGs may be used to determine the Bragg peak location via a simple mathematical relation. The distance between the Bragg peak location (x_{Bragg}) and the PG peak (x_{PG}), specified as Δ, is calculated for different proton beam energies. As can be seen in Table 3 and Fig. 23, although both x_{Bragg} and x_{PG} values increase with proton beam energy, the distance between the two peaks remains almost constant, which means that the Bragg peak location can be simply determined by careful detection of the proton-induced PGs and adding the value of ~3.7 cm to the location of the PG peak.

The accuracy of the penetration depth determination for protons and other high-energy ion beams can be improved by using more appropriate mathematical models which best describe the PG behavior along the phantom axis.

Table 3
The distance between the Bragg- and PG peaks (Δ) for different proton beam energies.

Proton energy (MeV)	Peak location (cm)		$\Delta = x_{Bragg} - x_{PG}$
	x_{PG}	x_{Bragg}	
110	5.38	9.05	3.67
120	6.93	10.62	3.69
130	8.30	12.00	3.70
140	10.14	13.81	3.67
150	11.83	15.55	3.72

Declaration of competing interest

The authors declare that they have no known competing financial interests or personal relationships that could have appeared to influence the work reported in this paper.

Data availability

Data will be made available on request.

Acknowledgment

This work was supported by grant No. 3/50008 (29/11/1398) from the Vice President for Research and Technology of Ferdowsi University of Mashhad.

References

[1] A. Ansarinejad, New generation of medical accelerators used in hadrontherapy, J. Radiat. Nucl. Technol. 2 (4) (2016) 18–27.
[2] A. Facoetti, A. Barcellini, F. Valvo, M. Pullia, The role of particle therapy in the risk of radio-induced second tumors: A review of the literature, Anticancer Res. 39 (9) (2019) 4613–4617.
[3] U. Amaldi, M. Dosanjh, B. Singers Sørensen, M. Scholz, J. Balosso, J. Overgaard, S. Rossi, A Facility for Tumour Therapy and Biomedical Research in South-Eastern Europe (No. CERN-2019-002), CERN, 2019.
[4] M. Moteabbed, S. Espana, H. Paganetti, Monte Carlo patient study on the comparison of prompt gamma and PET imaging for range verification in proton therapy, Phys. Med. Biol. 56 (4) (2011) 1063.
[5] C. Richter, G. Pausch, S. Barczyk, M. Priegnitz, I. Keitz, J. Thiele, J. Smeets, F. Vander Stappen, L. Bombelli, C. Fiorini, L. Hotoiu, First clinical application of a prompt gamma based in vivo proton range verification system, Radiother. Oncol. 118 (2) (2016) 232–237.
[6] T. Werner, J. Berthold, F. Hueso-González, T. Koegler, J. Petzoldt, K. Roemer, C. Richter, A. Rinscheid, A. Straessner, W. Enghardt, G. Pausch, Processing of prompt gamma-ray timing data for proton range measurements at a clinical beam delivery, Phys. Med. Biol. 64 (10) (2019) 105023.
[7] H. Rohling, M. Priegnitz, S. Schoene, A. Schumann, W. Enghardt, F. Hueso-González, G. Pausch, F. Fiedler, Requirements for a Compton camera for in vivo range verification of proton therapy, Phys. Med. Biol. 62 (7) (2017) 2795.
[8] H. Paganetti, Range uncertainties in proton therapy and the role of Monte Carlo simulations, Phys. Med. Biol. 57 (11) (2012) R99.
[9] T. Werner, J. Berthold, W. Enghardt, F. Hueso-González, T. Kögler, J. Petzoldt, C. Richter, A. Rinscheid, K. Römer, K. Ruhnau, J. Smeets, Range verification in proton therapy by prompt gamma-ray timing (PGT): Steps towards clinical implementation, in: 2017 IEEE Nuclear Science Symposium and Medical Imaging Conference, NSS/MIC, IEEE, 2017, pp. 1–5.
[10] Y. Xie, E.H. Bentefour, G. Janssens, J. Smeets, F. Vander tappen, L. Hotoiu, L. Yin, D. Dolney, S. Avery, F. O'Grady, D. Prieels, Prompt gamma imaging for in vivo range verification of pencil beam scanning proton therapy, Int. J. Radiat. Oncol. Biol. Phys. 99 (1) (2017) 210–218.
[11] P. Dendooven, H.J.T. Buitenhuis, F. Diblen, P.N. Heeres, A.K. Biegun, F. Fiedler, M.J. Van Goethem, E.R. Van der Graaf, S. Brandenburg, Short-lived positron emitters in beam-on PET imaging during proton therapy, Phys. Med. Biol. 60 (23) (2015) 8923.
[12] F.M.F.C. Janssen, G. Landry, P.C. Lopes, G. Dedes, J. Smeets, D.R. Schaart, K. Parodi, F. Verhaegen, Factors influencing the accuracy of beam range estimation in proton therapy using prompt gamma emission, Phys. Med. Biol. 59 (15) (2014) 4427.
[13] L.S. Waters, MCNPX User's Manual, Los Alamos National Laboratory, 2002, p. 124.
[14] M. Tajik, N. Ghal-Eh, G.R. Etaati, H. Afarideh, Modeling NE213 scintillator response to neutrons using an MCNPX-PHOTRACK hybrid code, Nucl. Instrum. Methods Phys. Res. A 704 (2013) 104–110.
[15] S. Min, Y. Kim, K.H. Ko, B. Seo, J. Cheong, C. Roh, S. Hong, Optimization of plastic scintillator for detection of Gamma-rays: Simulation and experimental study, Chemosensors 9 (9) (2021) 239.
[16] S. Min, K.H. Ko, B. Seo, J. Cheong, C. Roh, S. Hong, Wireless backpack system for detection of radioactive cesium on contaminated soil using portable plastic scintillator with efficient readout device, Electronics 10 (22) (2021) 2833.
[17] A.B. Clegg, K.J. Foley, G.L. Salmon, R.E. Segel, Gamma radiation from the medium energy proton bombardment of lithium, beryllium, boron, carbon and nitrogen, Proc. Phys. Soc. (1958-1967) 78 (5) (1961) 681.
[18] K.J. Foley, G.L. Salmon, A.B. Clegg, Gamma radiation from the bombardment of ^{16}O and ^{19}F nuclei with 150 MeV protons, Nucl. Phys. 31 (1962) 43–52.
[19] F.L. Lang, C.W. Werntz, C.J. Crannell, J.I. Trombka, C.C. Chang, Cross sections for production of the 15.10-MeV and other astrophysically significant gamma-ray lines through excitation and spallation of ^{12}C and ^{16}O with protons, Phys. Rev. C 35 (4) (1987) 1214.
[20] A. Belhout, S. Ouichaoui, H. Beaumevieille, A. Boughrara, S. Fortier, J. Kiener, J.M. Maison, S.K. Mehdi, L. Rosier, J.P. Thibaud, A. Trabelsi, Measurement and DWBA analysis of the $^{12}C(^{6}Li, d)^{16}O$ α-transfer reaction cross sections at 48.2 MeV. R-matrix analysis of $^{12}C(\alpha, \gamma)^{16}O$ direct capture reaction data, Nuclear Phys. A 793 (1–4) (2007) 178–211.
[21] J. Narayanaswamy, P. Dyer, S.R. Faber, S.M. Austin, Production of 6.13-MeV gamma rays from the $^{16}O(p, p' \gamma)^{16}O$ reaction at 23.7 and 44.6 MeV, Phys. Rev. C 24 (6) (1981) 2727.
[22] C. Toramatsu, E. Yoshida, H. Wakizaka, A. Mohammadi, Y. Ikoma, H. Tashima, F. Nishikido, A. Kitagawa, K. Karasawa, Y. Hirano, T. Yamaya, Washout effect in rabbit brain: In-beam PET measurements using ^{10}C, ^{11}C and ^{15}O ion beams, Biomed. Phys. Eng. Express 4 (3) (2018) 035001.